Designing Efficient Single-Atom Alloy Catalysts for Selective C=O Hydrogenation: A First-Principles, Active Learning and Microkinetic Study

Haisong Feng,[1,2] Meng Zhang,[1] Zhen Ge,[1] Yuan Deng,[1] Pengxin Pu,[1] Wenyu Zhou,[2,3] Hao Yuan,[2] Jing Yang,*[,2] Feng Li,[1] Xin Zhang,*[,1] and Yong-Wei Zhang*[,2]

[1] State Key Laboratory of Chemical Resource Engineering, Beijing Advanced Innovation Center for Soft Matter Science and Engineering, Beijing University of Chemical Technology, Beijing 100029, P. R. China

[2] Institute of High Performance Computing (IHPC), Agency for Science, Technology and Research (A*STAR), 1 Fusionopolis Way, #16-16 Connexis, Singapore 138632, Republic of Singapore

[3] School of Chemistry and Chemical Engineering, Chongqing University, Chongqing 401331, P. R. China

* Corresponding authors: Yang_Jing@ihpc.a-star.edu.sg (J. Yang); zhangxin@mail.buct.edu.cn (X. Zhang); zhangyw@ihpc.a-star.edu.sg (Y. W. Zhang).

ABSTRACT: Selective hydrogenation of α,β-unsaturated aldehydes into unsaturated alcohols is a process in high demand in organic synthesis, pharmaceuticals, and food production. This process requires the precise hydrogenation of C=O bonds, a challenge that requires a tailored catalyst. Single-atom alloys (SAAs), where individual atoms of one metal are distributed in a host metal matrix, offer a potential solution to this challenge. Nevertheless, identifying the appropriate SAA capable of targeted adsorption and efficient activation of C=O bonds remains a substantial hurdle. In this work, we synergistically combine density functional theory (DFT) calculations, active learning, and microkinetic simulation to design SAAs for the efficient and selective hydrogenation of α,β-unsaturated aldehydes. We first comprehensively assessed the potential of 66 SAAs across 264 surfaces (including (100), (110), (111) and (320) crystal planes), to gauge their potential in activating C=C and C=O bonds. Our assessment unveiled the excellent selectivity of the Ti_1Au SAA in activating C=O bonds. Moreover, our detailed DFT calculations further demonstrated the high catalytic activity of $Ti_1Au(320)$ and $Ti_1Au(111)$ surfaces with a low activation energy barrier of only 0.60 eV. Subsequently, we conducted microkinetic simulations on the selective hydrogenation process of crotonaldehyde, by selecting Ti_1Au (320) and (111) surfaces as the catalysts and demonstrated that they exhibited a remarkable selectivity and nearly 100% conversion towards crotyl alcohol in the temperature range from 373 to 553 K. The present study not only reveals novel SAAs for targeted hydrogenation of α,β-unsaturated aldehydes but also establishes a promising path towards efficient design of selective hydrogenation catalysts more broadly.

KEYWORDS: *Single-atom alloy catalysts,* C=O *selective hydrogenation, density functional theory, active learning, microkinetic simulations*

■ INTRODUCTION

Given the theme of sustainable development in the fields of economy and environment, achieving catalytic transformation of specific functional groups remains a long-standing goal of the catalysis community.[1–4] Catalytic selective hydrogenation, crucial for producing organic intermediates and effectively purifying products, is of paramount importance in chemical, pharmaceutical and petrol industries.[5–10] In particular, the selective hydrogenation of α,β-unsaturated aldehydes to unsaturated alcohols is widely demanded in the fields of organic synthesis, pharmaceutical industries and foods, thus attracting significant attention.[11–14] However, the targeted hydrogenation of C=O bonds in α,β-unsaturated aldehydes to form unsaturated alcohols is extremely challenging due to the thermodynamic and kinetic preference for hydrogenation of the conjugated C=C bond over the C=O bond. [15–17] Many efforts have been dedicated to addressing this issue, and a great amount of research has focused on the design of catalysts that selectively activate the C=O bond to improve the selectivity toward unsaturated alcohols.

Extensive research[18-25] has shown that the adsorption mode of the unsaturated aldehyde on the catalyst surface plays a pivotal role in the selectivity in the hydrogenation of unsaturated aldehydes. More active metals, such as Ni, Pd, and Pt, form stronger interactions with C=C bonds, making them easier to activate.[26-28] In contrast, less reactive metals, such as Ag, Au, and Cu, are expected to have weaker interactions with α,β-unsaturated aldehydes, resulting in higher selectivity for unsaturated alcohols. However, their weak activity can be attributed to a limited ability for hydrogen activation.[29-31] This balance between reactivity and selectivity is a crucial factor in catalyst design. Various strategies have been employed to engineer the adsorption mode of the unsaturated aldehyde: (1) Utilizing confinement and steric effects: This strategy hinders the adsorption of the C=C bond

usually located in the middle of the molecule, but favors the adsorption of the C=O bond located at the terminal end of the molecule;[18–20] (2) modulating the electronic structure of the active site: This strategy diminishes the adsorption of the C=C bond as the electron density of the active metal increases;[21–23] (3) designing targeted adsorption sites: This strategy enables specific adsorption of C=O bonds.[24,25] Thereinto, the most straightforward and efficient approach is to design catalysts with tailored active sites for C=O bond adsorption. Among all the catalysts, the SAAs, where a small fraction of an active metal is meticulously isolated on the surface of an inert-metal host, stand out as the most promising and captivating contenders. The pioneering experiments conducted by Zaera and Trenary et al. provided initial evidence of the remarkable potential of SAAs in the selective hydrogenation of unsaturated aldehydes.[24,25,32] Subsequent theoretical investigations provided additional support to the significant role of SAAs in the realm of selective hydrogenation of unsaturated aldehydes by controlling host-guest metals to achieve specific adsorption on C=O bonds.[33] Hence, the exploration of various single atoms and the development of an efficient method to identify highly promising candidate catalysts from a broad array of SAAs for the selective hydrogenation of unsaturated aldehydes hold immense fundamental and technological significance.

Unfortunately, achieving the aforementioned goal solely through experiments and density functional theory (DFT) calculations proves to be unfeasible due to the vast array of components and compositions. This diversity results in an immense size of the design space. Currently, by integrating DFT with advanced machine learning (ML) algorithms, specifically aimed at predicting adsorption energy, a pioneering approach emerges in the quest for uncovering the optimal composition of bimetallic alloys.[34–36] The combination of DFT calculations with ML potential effectively overcomes the limitations of each method. DFT calculations enable the consideration of complicated potential

energy surfaces involving various surface reactions, whereas ML allows for large-scale predictions and provides valuable insights into the structure-activity relationships of catalysts. Notably, active learning possesses the remarkable ability to substantially decrease the necessary training data size by multiple orders of magnitude, offering a convenient avenue for investigating complex chemical conundrums.[37–40] This development enables efficient exploration and understanding of intricate chemical problems with enhanced precision and reduced computational burden. Therefore, the synergy between DFT calculations and active learning offers a promising new avenue for achieving breakthroughs in SAAs design.

In this work, we demonstrate an effective methodology that combines DFT calculations with active learning, aimed at identifying the optimal composition of SAA catalysts specifically for the selective hydrogenation of crotonaldehyde (CRAL). To do so, we focus on three host metals, Cu, Ag, and Au, due to their inertness, which minimally affects the adsorption mode of unsaturated aldehydes. The attainment of the optimal catalysts is achieved by adjusting the species and coordination numbers of SAAs. The following distinct coordination numbers of SAAs are considered: 9 for M_1Cu/Ag/Au(111), 8 for M_1Cu/Ag/Au (100), 7 for M_1Cu/Ag/Au (110) and 6 for M_1Cu/Ag/Au (320). In the initial stage, 528 adsorption free energies on 264 surfaces were systematically investigated using a combination of DFT calculations and active learning predictions. A promising candidate catalyst, Ti_1Au SAA, was successfully identified for the selective hydrogenation of unsaturated aldehydes. Next, detailed mechanistic studies by DFT calculations revealed that both the (320) and (111) surfaces displayed remarkably low energy barriers (less than 0.6 eV) for the hydrogenation of C=O bonds, highlighting their exceptional activity of the Ti_1Au catalysts. Finally, the microkinetic simulations conclusively demonstrate that both Ti_1Au(111) and Ti_1Au(320) exhibit high selectivity

and great potential for the selective hydrogenation of unsaturated aldehydes.

■ METHODS

Density Functional Theory Calculations. The first-principles calculations were performed using the Perdew-Burke-Ernzerhof (PBE)[41] functional within the generalized gradient approximation (GGA) in the Vienna Ab initio Simulation Package (VASP 5.4.4).[42,43] To account for van der Waals forces, the D3 dispersion correction with Becke-Johnson damping was incorporated in the DFT calculations.[44] The core-valence electron interaction was represented using the projector-augmented wave (PAW) method.[45,46] The structures were optimized until the forces acting on all atoms are below 0.02 eV $Å^{-1}$ and the energies are below 10^{-5} eV, ensuring the convergence and reliability of the results. The transition state was explored using the dimer[47] and climbing image nudged elastic band (CI-NEB)[48] methods, followed by verification through vibration frequency calculations. Only one imaginary frequency was identified, confirming the authenticity and uniqueness of the transition state.[49] To ensure the accuracy and reliability of the DFT calculations for the metal surfaces, a cutoff energy of 400 eV was chosen for the plane-wave basis set. To accurately sample the Brillouin zone, a 10 × 10 × 10 grid was used for bulk metal in the Monkhorst−Pack scheme, a 3 × 3 × 1 *k*-point mesh was used for (100) and (111) surfaces, and 2 × 3 × 1 and 2 × 2 × 1 *k*-point meshes were used for (110) and (320) surfaces, respectively. For electronic structure calculations, a 5 × 5 × 1 *k*-point mesh was adopted.

Copper (Cu), silver (Ag), and gold (Au), all of which fall within the cubic crystal system, were selected as the primitive cells for our model. Detailed parameters of the unit cell are provided in Table S1. For the surface models, a $p(4 \times 4)$ slab was used for the (100) and (110) surfaces; a $p(5 \times 5)$ slab was used for the (111) surface; and a $p(4 \times 2)$ slab was used for the (320) surface. All the slabs

consisted of at least 4 layers, and the bottom two layers were fixed during structure optimization. To ensure sufficient separation between periodic images, a vacuum layer of 15 Å was included for all surfaces. SAAs models were built by substituting one surface atom in the unit cell with the designated dopant atom. The coordination numbers of single-atom metals on the (111), (100), (110), and (320) surfaces are 9, 8, 7, and 6, respectively.

The Gibbs free energy of the adsorption states and the surface reaction mechanism were calculated under common reaction condition (373 K) [12,50]. Gibbs free energy was calculated as Eq. (1):

$$G = H - TS = E_{\mathrm{DFT}} + E_{\mathrm{ZPE}} - TS \quad (1)$$

where $E_{\mathbf{DFT}}$ is the static electron energy of the system at 0 K. $E_{\mathbf{ZPE}}$ is the zero-point energy correction. E_{H} is the enthalpy contribution of the system. T is the reaction temperature. S is the entropy of the adsorbate. The free energy change of adsorption was calculated as Eq. (2):

$$\Delta G_{\mathrm{ads}} = G_{\mathrm{total}} - (G_{\mathrm{gas}} + G_{\mathrm{slab}}) \quad (2)$$

where G_{total} is the total Gibbs free energy of the system with an attached adsorbate, G_{gas} is the Gibbs free energy of the gas phase adsorbate, and G_{slab} is the Gibbs free energy of the slab.

The Gibbs free energy barrier ($\Delta G^{\neq}$) of a reaction on SAAs surface is calculated as Eq. (3):

$$\Delta G^{\neq} = G_{\mathrm{transition\ state}} - G_{\mathrm{reactant}} \quad (3)$$

where $G_{\mathrm{transition\ state}}$ is the Gibbs free energy of the transition state, and G_{reactant} is the Gibbs free energy of the reactant.

Machine learning. All machine learning algorithms were implemented using the open-source *Scikit-learn* package[51] in the *Python3* environment. In this study, four distinct supervised machine

learning algorithms were chosen, including AdaBoost Regressor (ABR), Gradient Boosting Regressor (GBR), Random Forest Regressor (RFR), and Gaussian Process Regressor (GPR). The objective is to develop a well-trained model capable of accurately predicting the adsorption energies of various adsorption configurations. The performance of the ML models is evaluated using the root-mean-square error (RMSE) and the coefficient of determination values (R^2 score). The RMSE and R^2 score were calculated based on Eq. (4) and Eq. (5), respectively:

$$RMSE = \sqrt{\frac{1}{n}\sum_{i=1}^{n}(y_i - \dot{y}_i)^2} \tag{4}$$

$$R^2 = 1 - \frac{\sum_{i=1}^{n}(y_i - \dot{y}_i)^2}{\sum_{i=1}^{n}(y_i - \bar{y}_i)^2} \tag{5}$$

where $\dot{y}_i$ is the ground truth, y_i is the prediction of the model and $\bar{y}$ is the mean value.

Previous study[52] demonstrated the efficacy of utilizing the physicochemical properties, including atomic number (*N*_s), radius (*R*_s), valence (*V*_s), electronegativity (*E*_s), electrophilicity (*Ea*_s), and first ionization energy (*F*_s) for single atom metals as well as atomic number (*N*_h), radius (*R*_h), valence (*V*_h), electronegativity (*E*_h), electrophilicity (*Ea*_h), and first ionization energy (*F*_h) for host metals. These features were also employed in the present study. In addition, considering the unique nature of this work, we also incorporated the relative atomic mass (*M*_s and *M*_h) of host-guest metals and coordination number (CN) of the single atom as new features. Furthermore, the numerical labels 1 and 2 were employed to distinguish the two adsorption configurations (named feature S). Considering the synergy that exists between host metals, the features in the initial feature set are systematically combined using a straightforward mathematical operation, involving the calculation of the mean and difference between the corresponding features, and all 30 features initially selected are shown in Table S2 and S3.

Microkinetic Simulations. Microkinetic simulations were performed by the MKMCXX program.[53,54] The forward and backward rate constants of the elementary steps were determined using Eq. (6):

$$k = \frac{k_B T}{h} \frac{Q^{TS}}{Q} e^{-G_a / k_B T} \tag{6}$$

where k_B, T, h, Q^{TS}, Q and G_a are the Boltzmann constant, temperature, Planck's constant, partition function of the transition state, partition function of the initial state, and activation barrier, respectively.

The molecular adsorption rate was determined using Eq. (7):

$$k_{ads} = \frac{PA}{\sqrt{2\pi m k_B T}} S \tag{7}$$

where *P, A, S,* and *m* are the the partial pressure of the adsorbate, surface area, sticking coefficient and the mass of the adsorbate, respectively.

■ RESULTS AND DISCUSSION

Crotonaldehyde adsorption on the SAA surfaces. Extensive investigations, including both surface science studies and catalytic experiments, have been dedicated to exploring the adsorption characteristics of unsaturated alcohols, which plays an important role in modulating the selectivity of SAAs.[55,56] Regarding possible adsorption geometries, two distinct configurations, corresponding to interactions with either functional group, exhibit energy minima on SAA guest sites.[33] To enrich the breadth of our constructed ML dataset, we initially focused on 10 diverse metals (including Ti, Fe, Mo, Ru, Rh, Pd, Ta, Re, Ir and Pt) from varying periods and groups as single-atom constituents. With these elements in focus, we delved into the exploration of the two adsorption configurations of

CRAL through DFT calculations. As shown in Figure 1a–d, the investigated geometries encompass the π_{CO} and π_{CC} configurations, both of which are adsorbed at the top sites of single atoms. For the π_{CO} configuration, the C=O bond is adsorbed directly at the top site of the single atom, with the O atom positioned approximately 1.90 Å away from the single atom. Meanwhile, the C=C bond maintains a notable distance from the catalyst surface (with the closest distance exceeding 2.50 Å). This configuration potentially circumvents the activation of the C=C bond, thus favoring the formation of crotyl alcohol (CROL). Conversely, in the adsorption configuration, the C=C bond is positioned atop the single atom, while the C=O bond remains distanced from the active center. This arrangement is conducive to the generation of butyraldehyde (BUAL). The calculated Gibbs free energies of adsorption results unveiled a distinct trend: earlier transition metals exhibited robust adsorption on CRAL, while late transition metal displayed weaker affinity towards CARL (Figure 1e and Table S4). For example, on the $Ta_1Cu(111)$ surface, the adsorption energies for the π_{CO} and π_{CC} configurations are −1.95 and −1.23 eV, respectively, whereas on the Pt_1Cu111 surface, they stand at −0.07 and −0.36 eV, respectively. Comparative analysis of the Gibbs free energies of adsorption for the two configurations shows that alkenes prefer to bind on late transition metal sites, while earlier transition metals prefer aldehyde modes, leading to strong overall adsorption. Additionally, the surfaces with low single-atom coordination numbers, such as the (320) surface, exhibit stronger adsorption capacities and more pronounced differences in adsorption energy, indicating their potential for high catalytic activity. Therefore, early transition metal SAAs are promising candidates for the selective hydrogenation of unsaturated aldehydes to unsaturated alcohols.

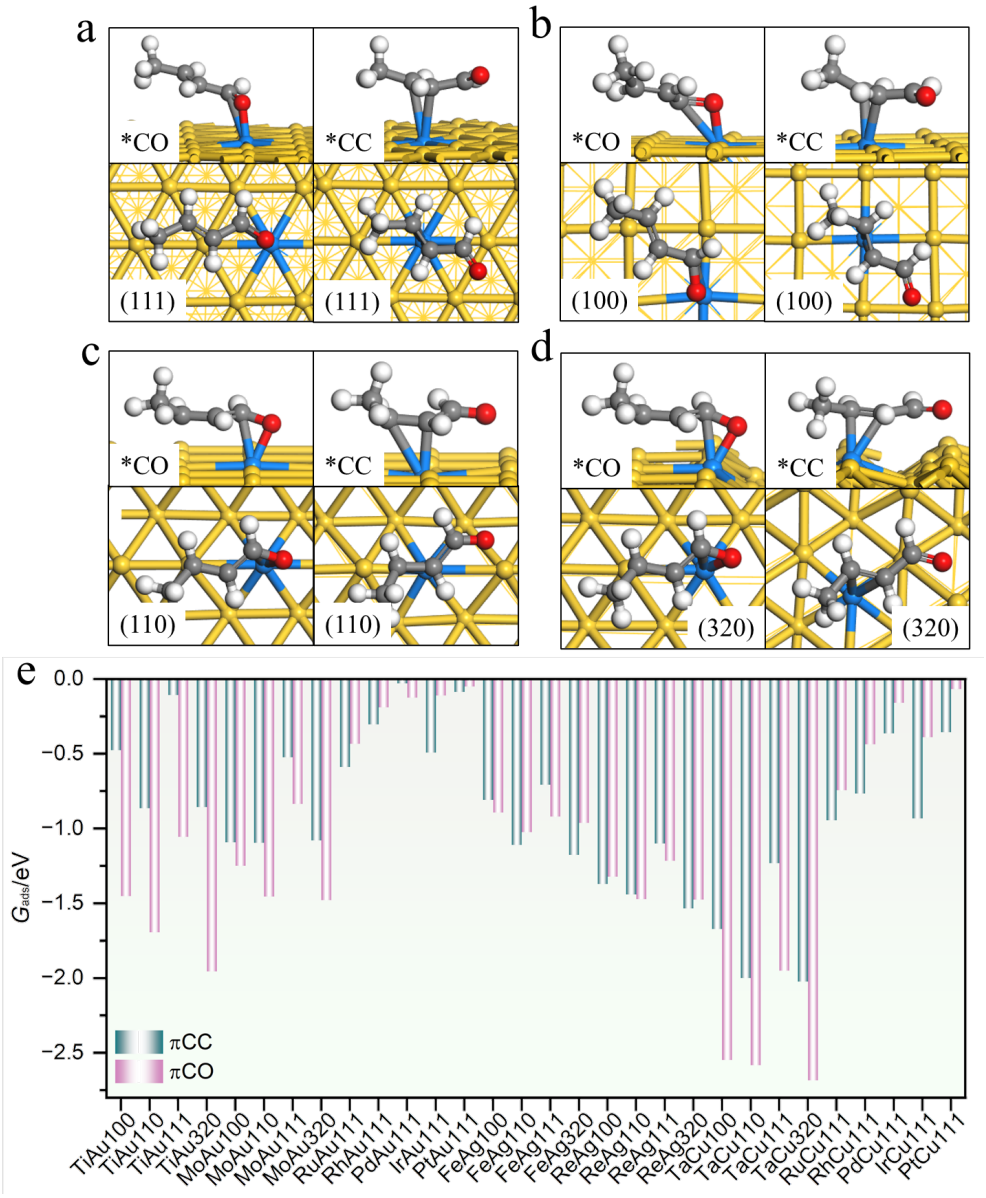

Figure 1. (a-d) The adsorption configurations of crotonaldehyde on the M_1M_{host} (100), (110), (111) and (320) surfaces (the left side presents a schematic diagram of the adsorption configuration with the C=O bond adsorbed at the top site of a single atom, while the right side displays a schematic diagram of the adsorption configuration with the C=C bond adsorbed at the top site of a single atom). (e) Gibbs free adsorption energy of crotonaldehyde on SAA surfaces.

Active-Learning Framework Construction. In order to explore more potential SAA catalysts,

we use up to 60 adsorption free energies calculated by DFT as the initial data set to construct an active learning framework (Scheme 1). Initially, the model was trained using a smaller dataset to make preliminary predictions. While continually evaluating the model's uncertainty and errors, we strategically conducted DFT calculations on data points with higher uncertainty to effectively supplement the dataset. This iterative process continued until the model's uncertainty and error reached the desired ideal values, at which point the iteration was terminated. This framework improves model performance by selectively identifying and labeling the most informative samples, thereby minimizing the need for extensive data labeling while achieving highly accurate predictions.

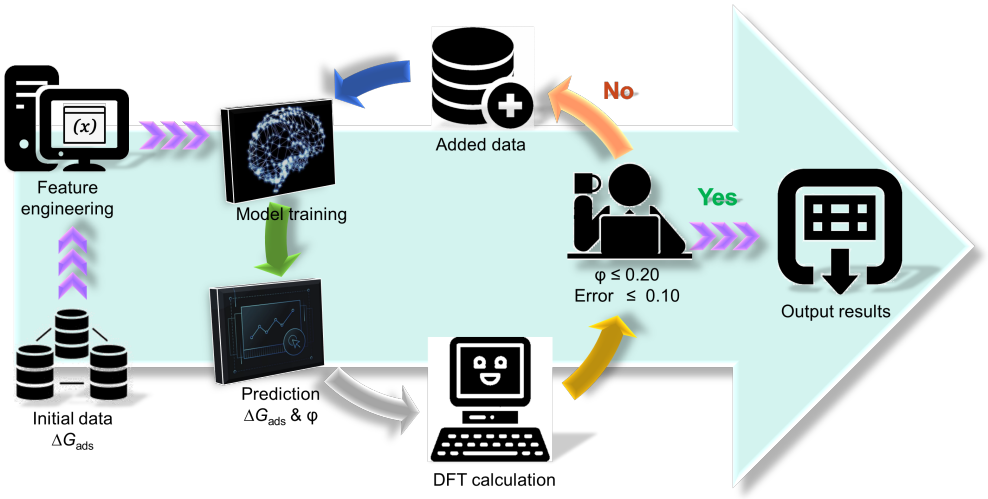

Scheme 1. The overall workflow of active learning (φ represents uncertainty).

Generally, the creation of an ideal feature set is pivotal in constructing a ML model with high precision. Balancing the selection of features is crucial, as an excessive number of features can result in redundancy, while an insufficient number of features may fail to meet the fundamental requirements for model establishment. Therefore, the Pearson correlation analysis was conducted to examine the interrelationships among the 30 initial features, the results are shown in Figure S1. It is seen that there are many highly correlated features, and an excessive number of such attributes could

potentially trigger the “curse of dimensionality”, thereby augmenting the susceptibility to overfitting.[57,58] To obtain the optimal features, the feature recursive elimination (FRE) method was employed to refine the initial feature set. The FRE score serves as a metric to gauge the effectiveness of a feature in describing the target value, with higher scores indicating a stronger correlation between the feature and the target. As shown in Figure 2a, when the number of features is six, the FRE score reaches its peak, indicating the optimal subset of features for the given analysis. The majority of these six characteristics exhibit low correlations (Figure 2b), suggesting that the selected features are both reasonable and indispensable for the analysis at hand. To comprehend the relationship between the features and the targeted property (adsorption free energy), the degree of the importance of the six selected features was evaluated. The evaluation results show that the E_s emerges as the most influential factor in determining the adsorption free energy, contributing approximately 35% to the overall predictive model. The remaining factors accounted for values ranging from 6.8% to 19.9% as shown in Figure 2c. The similar degree of importance observed among the evaluated features further reinforces the validity of our feature selection process. Hence, the combination of these six features along with the dataset of 60 adsorption free energy values will be employed to construct a robust machine learning model.

Identifying the best fitted model for a specific dataset also holds paramount significance in achieving a high-precision ML model. In this study, four ML models (ABR, GBR, GPR and RFR) were chosen for initial evaluation. The optimal hyperparameters are obtained through an automated hyperparameter search process (Table S5), ensuring that the model is fine-tuned for optimal performance. Based on the statistical analysis of 100 training results, all four models have exhibited excellent performance (Figure 2d and Figure S2). Notably, both the training set and the test set

achieved a high R^2 score exceeding 0.88, while the corresponding RMSE remained below 0.20 eV. Among the four models, the GPR model exhibited the best performance, with R^2 scores over 0.97 and low RMSE values below 0.11 eV in both of model training and test phases. Furthermore, the GPR model is able to assess the uncertainty of its predictions, which is represented by the diagonal elements of the covariance matrix. This feature holds great significance in the active-learning framework, as it enables a comprehensive understanding of the confidence and reliability of the model's predictions. Therefore, the GPR model is employed in the subsequent active learning process.

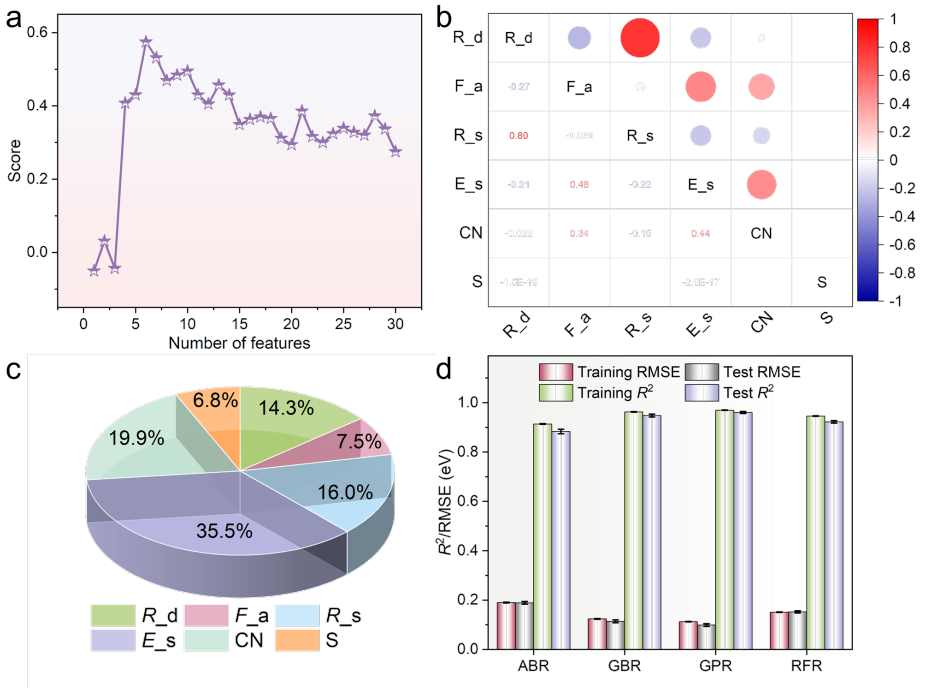

Figure 2. (a) The relationship between the number of features and the score of the model in the RFE method. (b) Pearson correlation map between the 6 input features. (c) Feature importance for the Gibbs free energy of adsorption. (d) The distribution of the R^2 score and RMSE for the four ML models in 100 repeated trials.

During the active learning iterations, the model generates two distinct types of outputs for each candidate SAAs: the adsorption free energy values for both the π_{CC} and π_{CO} adsorption configurations of crotonaldehyde; and the estimated uncertainty associated with each prediction. For the initial round of machine learning predictions, the model encountered a lack of sufficient training data, leading to considerably high uncertainty in its prediction results. As shown in Figures S3–S10, the uncertainty in the initial round of ML predictions was over 0.50 eV, indicating a significant uncertainty associated with the model's predictions. In regions displaying notable uncertainties, a subset of 10 representative data points with large uncertainties was carefully chosen for verification through DFT calculations. The results of these calculations and their corresponding predictions are shown in Figure 3a. The maximum errors observed between the DFT calculations and machine learning predictions reach nearly 1.00 eV ($G_{ads\_\pi CC}$ on FeAu(320) and $G_{ads\_\pi CO}$ on HfAg(320)), underscoring the imperative need for the subsequent round of machine learning iterations. The significant uncertainty and error in the ML predictions may be attributed to the limited number of data points available in this specific area of the dataset. Consequently, incorporating these additional data points into the dataset has the potential to greatly enhance the prediction accuracy of ML. Upon adding these 10 data points to the dataset, the model training results retained its excellent performance, with an R^2 value of 0.95 and an RMSE of 0.12 eV for the test set (Figure S11). It is worth noting that the maximum uncertainty of the ML prediction results has been reduced to 0.35 eV (Figures S12–S19). The verification results of DFT for the adsorption energy in the region of maximum uncertainty demonstrate a prediction error of approximately 0.50 eV (Figure 3b), suggesting that the performance of the model has been improved in the second iteration. Despite the improvement, the error of 0.50 is still unsatisfactory, prompting us to conduct a third round of ML.

Following the third round of model training and optimization, the uncertainty of machine learning prediction was further reduced to 0.20 eV, with the maximum prediction error reaching only 0.10 eV (Figures S20–S28 and Figure 3c). The maximum uncertainty associated with the prediction results witnessed a steady decline, indicating the increased accuracy and reliability of our model. Furthermore, the analysis of dataset distribution at each round of ML, as well as the overall dataset distribution (Figure S29), reveals that the inclusion of new data progressively aligns the dataset distribution with the overall data distribution. This convergence further validates the rationality and effectiveness of our final dataset.

After the completion of the active learning iterations, we obtained a comprehensive data comprising 528 adsorption free energies corresponding to 264 SAA surfaces (Figure 3d–f). The activation ability of C=O bond and C=C bond was judged by comparing the adsorption preference of SAAs to π_{CO} and π_{CC} modes. On most SAA surfaces, the adsorption in π_{CO} mode is more stable thermodynamically. Among them, when Sc, Y, Zr, Nb, Hf, and Ta are employed as single-atom metals, the adsorption energy of the π_{CO} adsorption mode is found to be lower than −1.10 eV, indicating its greater potential for activating C=O bonds. Only a few noble metal SAA surfaces exhibit greater stability in the π_{CC} mode, facilitating the easier activation of C=C bonds. Among these SAAs, the Ti_1Au exhibits the largest disparity in adsorption energy between the two modes with a preference of π_{CO} mode adsorption ($\Delta G_{ads} = G_{ads\_\pi CO} - G_{ads\_\pi CC} = 1.10$ eV).

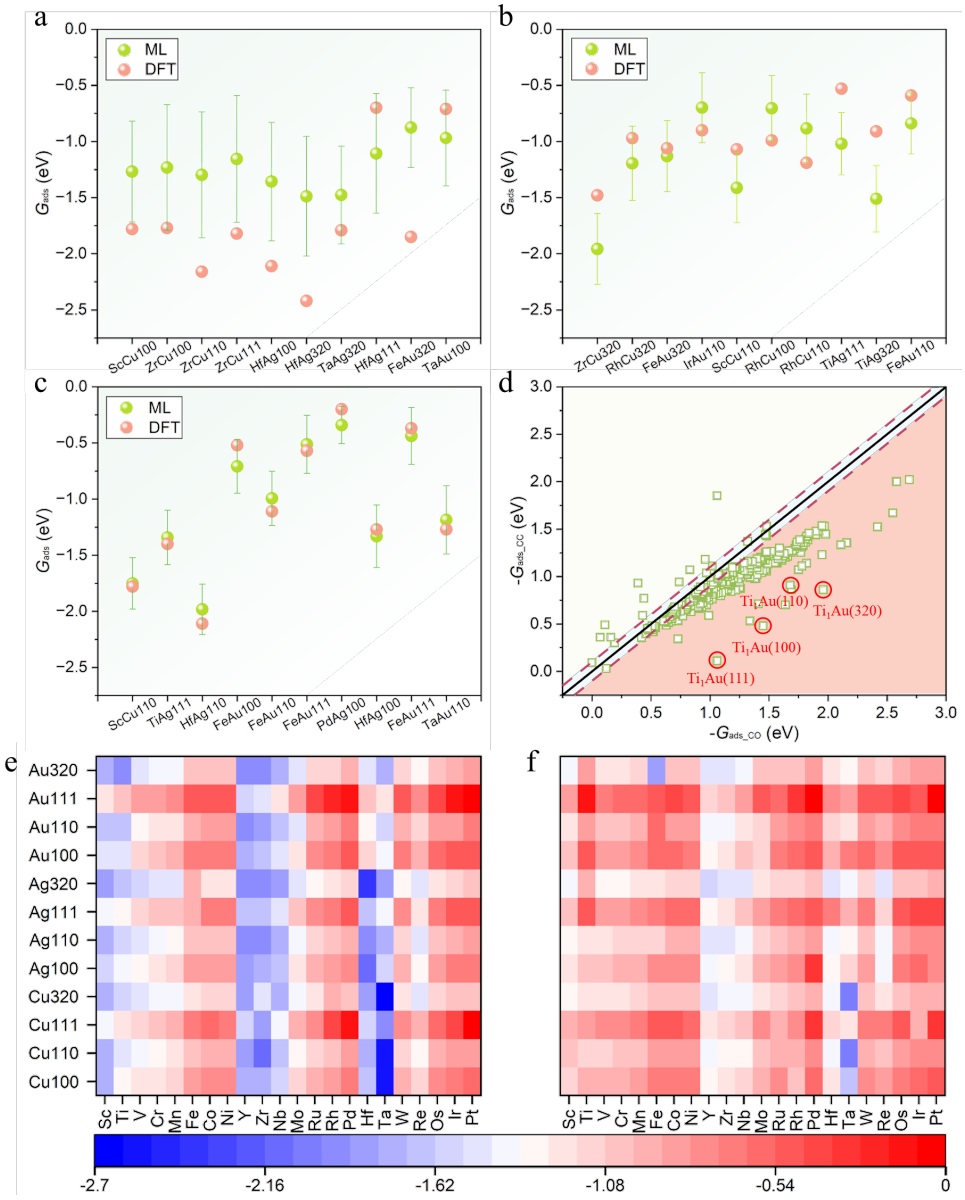

Figure 3. Comparison of predicted values of 10 high-uncertainty points by active learning with DFT calculated values in (a) 1st round, (b) 2nd round and (c) 3rd round machine learning. (d) The adsorption free energy of π_{CO} and π_{CC} modes on the SAA surfaces (The black solid line indicates the same adsorption free energy for the two adsorption modes, and the red dashed line indicates the prediction error of 0.10 eV). Heat map of ML-predicted adsorption free energy for (e) π_{CC} mode and (f) π_{CO} mode.

Feature Importance Analysis. To evaluate the relationship between features and target property, we employed three evaluation metrics: Pearson Correlation Coefficient (PCC), Spearman Correlation Coefficient (SCC), and Mutual Information (MI) (Figure 4a). All three methods yielded consistent results, showing that CN, *F*_a, and *E*_s exhibited stronger correlations with the adsorption free energy. Furthermore, we investigated the influence of different features on the adsorption energy separately for the two adsorption modes (Figure 4b, c). The results show that the features with the highest correlation to the adsorption energy is *E*_s for the π_{CO} adsorption mode. In contrast, for the π_{CC} adsorption mode, the feature with the highest correlation is CN. This discrepancy could be attributed to the pronounced electrophilicity exhibited by the oxygen atom in the C=O bond, which significantly influences its adsorption behavior. To better understand the influence of host-guest metal properties on adsorption energy, we deconstructed composite features such as *F*_a and *R*_d (Figure 4d, e). This approach allows us to differentiate the unique contributions of the host and guest metals, providing a more comprehensive understanding of their individual impacts on adsorption energy. As anticipated, our findings demonstrate that the characteristics of single metal atoms exhibit a stronger correlation with the adsorption free energy compared to those of host metals, which holds true for both adsorption modes.

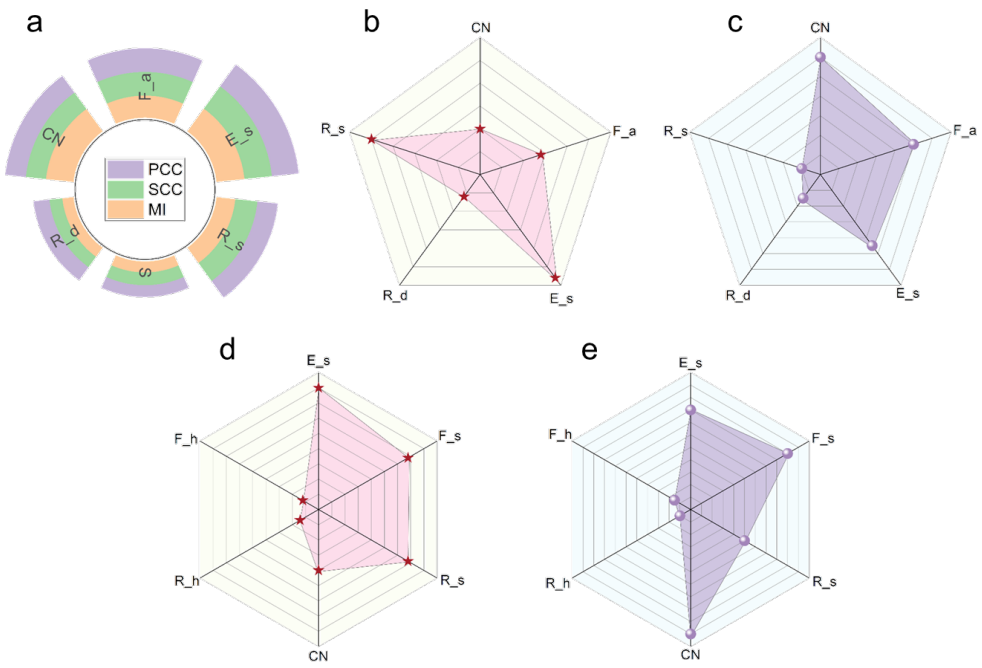

Figure 4. (a) Feature importance analysis by PCC, SCC and MI. Importance analysis of 5 features selected for machine learning for (b) G_{ads}_π_{CO} and (c) G_{ads}_π_{CC}. Importance analysis of 6 features selected for machine learning for (d) G_{ads}_π_{CO} and (e) G_{ads}_π_{CC}. (*R*_s, *E*_s, *R*_d, *F*_a, *CN* and *S* represent the radius of the guest metal, the electronegativity of the guest metal, the radius difference between the host and guest metal, the average value of the first ionization energy of the host and guest metal, the coordination number of the guest metal and the adsorption mode.)

Investigations on the mechanism of crotonaldehyde hydrogenation over Ti_1Au SAA. Understanding the fundamental reasons behind the disparity in adsorption energy between the two adsorption configurations is essential in gaining insight into the underlying reaction mechanism. Hence, we conducted an exploration of the electronic structures associated with the two adsorption configurations of crotonaldehyde on the Ti_1Au surfaces. Figure 5a, 5b depicts the observed difference in charge density when crotonaldehyde is adsorbed on $Ti_1Au(320)$. In the π_{CC} adsorption mode, the charge accumulation primarily takes place between the C=C bond and the Ti atom. In

contrast, in the π_{CO} adsorption mode, the charge accumulation predominantly occurs between the C=O bond and the Ti atom, with a significantly higher accumulation compared to the former mode. This observation suggests that the C=O bond possesses a stronger interaction with the single-atom alloy surface compared to the C=C bond. Remarkably, (320) and (111) surfaces exhibit significantly larger electron transfer between the adsorbate and the surface, suggesting that they possess the highest catalytic activity compared to the other two surfaces. To delve deeper into the interaction between the C=C bond and C=O bond with the single-atom alloy surfaces, the Projected Density of States (PDOS) of Ti3*d*, C2*s*2*p* and O2*s*2*p* for the two adsorption configurations were calculated (Figure 5c, 5d and Figures S36–S41). In the case of the C=C bond to Ti atom, there is limited orbital overlap between the 3*d* orbital of Ti atom and the 2*s*2*p* orbital of C atoms. In contrast, when the C=O bond is adsorbed on Ti atom, there is a significant overlap between the 3d orbitals of Ti and the 2s2p orbitals of CO. This results in a strong coupling between the narrow Ti 3*d* orbitals and CO *sp* orbitals, highlighting a significant interaction between the two entities. The further Crystal Orbital Hamilton Population (COHP) analysis (Figure 5e, 5f) shows that the negative integral of COHP (−ICOHP) values corresponding to the bonding between the two C atoms in the C=C bond and Ti atom are 1.78 and 1.29 eV on the Ti_1Au(320) surface, respectively, indicating a similar binding strength between the two C atoms and Ti atom. However, the −ICOHP values corresponding to the bonding between the C/O in the C=O bond and Ti atom are 0.98 and 3.82 eV, respectively, indicating much stronger Ti-O bond than Ti-C bond. The results on the (100), (110) and (111) surfaces (Figures S42–S47) bear similarity to those observed for the (320) surface (Figures S30–S35). In addition, by calculating the *d*-band center values of Ti atoms on the Ti_1Au(111), (100), (110), and (320) surfaces and their correlation with the adsorption free energy and mode of π_{CC} and π_{CO} (Figure S48), we note that the

proximity of the *d*-band center of the Ti atom to the Fermi level is directly related to the stability of CRAL adsorption on Ti_1Au SAA surfaces. Remarkably, the *d*-band center of Ti atoms on the Ti_1Au (320) surface is the closest to the Fermi level, underscoring its robust adsorption capacity for CRAL. Based on the aforementioned electronic structure analysis, it can be concluded that Ti_1Au SAA exhibits a remarkable propensity for activating the C=O bond.

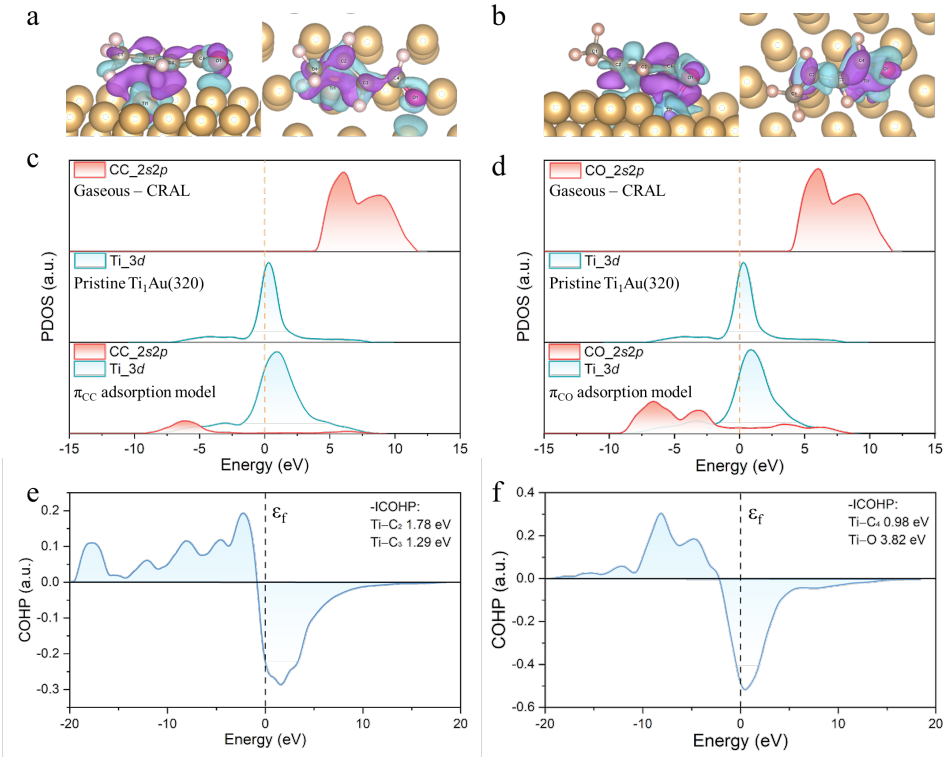

Figure 5. Charge density difference of crotonaldehyde adsorbed in (a) π_{CC} and (b) π_{CO} modes on $Ti_1Au(320)$ surface. (Purple and blue represent charge accumulation and depletion, respectively; the cutoff of the density-difference isosurface is 0.0032 e $Å^{-3}$). Projected density of states for (c) π_{CC} and (d) π_{CO} mode on $Ti_1Au(320)$ surface. The crystal orbital Hamiltonian populations (COHP) of Ti-C/O for (e) π_{CC} and (f) π_{CO} mode over $Ti_1Au(320)$ surface.

While adsorption plays a crucial role in catalytic cycles and can influence selectivity towards a particular pathway, it is essential to consider all downstream intermediates in the overall process. The

hydrogenation of CRAL leads to the formation of two distinct products: CROL by the hydrogenation of the C=O bond and BUAL by the hydrogenation of the C=C bond. Subsequently, the production of butanol (BUOL) is obtained through the sequential hydrogenation of either intermediate product, as depicted in Figure 6a. In the initial phase, the free energies of hydrogenation pathways for C=O bonds were calculated on the four surfaces of Ti_1Au SAA, yielding valuable insights into the energetics of the catalytic process. As shown in Figures S49–S53, the hydrogenation Gibbs free energy barriers (at 373 K) of the O atoms during the CRAL hydrogenation to CROL were found to be 0.50, 0.60, 0.69, and 0.96 eV on the (320), (111), (110), and (100) surfaces of Ti_1Au SAA, respectively. These barriers are higher than the hydrogenation barriers of C atoms (0.05 – 0.23 eV). These findings suggest that the Ti_1Au (320) and (111) surfaces exhibit higher catalytic activity than the (110) and (100) surfaces. Based on these observations, we conducted a more mechanistic study on the Ti_1Au (320) and Ti_1Au (111) surfaces.

The potential energy surfaces and intermediate configurations corresponding to the two different pathways involved in the hydrogenation of CRAL to either CROL or BUAL on Ti_1Au(320) and Ti_1Au(111) are presented together in Figure 6b and Figures S52–S54, providing a comprehensive visual representation of the reaction energetics. On the Ti_1Au(320) surface, the energy barriers for the initial hydrogen addition to the O atom in the C=O bond and the C atom in the C=C bond were determined to be 0.50 and 0.75 eV, respectively. The energy barriers for the second hydrogenation step were found to be 0.05 and 0.32 eV, respectively. The hydrogenation energy barrier for the C=C bond is more than 0.20 eV higher than that of the C=O bond, indicating that CROL products are more readily formed compared to BUAL products. A similar result is also observed on the Ti_1Au(111) surface. Subsequently, both CROL and BUAL undergo a two-step

hydrogenation process, overcoming an energy barrier of over 0.80 eV to produce the overhydrogenated product BUOL. The energy barrier for the formation of BUOL is significantly higher compared to that of C=O bond hydrogenation, suggesting that the formation of overhydrogenated products can be effectively suppressed. This finding further reinforces the notion that Ti_1Au SAA serves as an ideal candidate catalyst for the selective hydrogenation of CRAL to CROL.

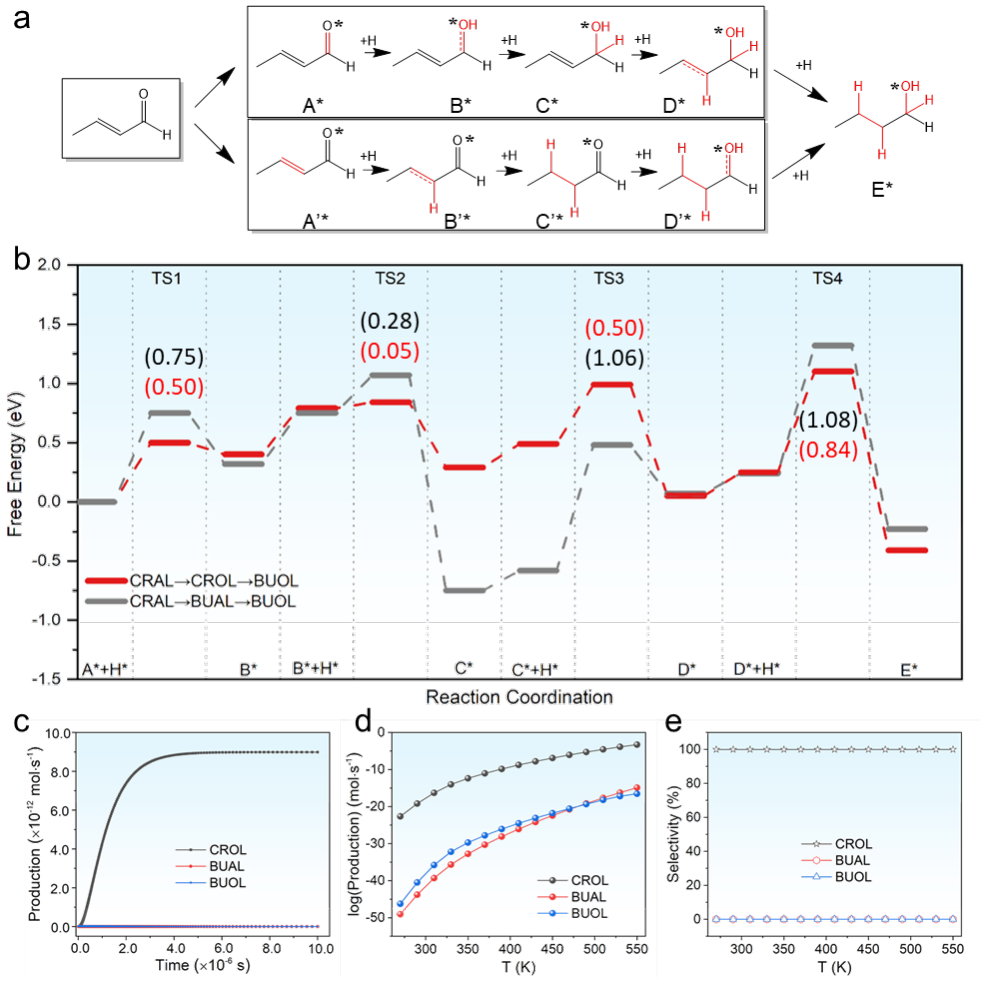

Figure 6 (a) Reaction network with two different elementary hydrogenation paths. (b) Free energy profiles of CRAL hydrogenation on $Ti_1Au(320)$ surface at 373 K. (c) Reaction rate predicted by the microkinetic simulations on $Ti_1Au(320)$ surface (T = 373 K, p = 2 atm). (d) Reaction rate and

(e) product selectivity prediction at different temperatures by the microkinetic simulations on $Ti_1Au(320)$ surface (p = 2 atm).

Table 1. The 14-step elementary reactions involved in the microkinetic simulation.

Elementary Reactions	Gr	G_{a_f}	G_{a_b}	Step
$H_2(g) + * \leftrightarrow H_2*$	0.03	NaN	NaN	r(1)
$H_2* + * \leftrightarrow 2H*$	−0.14	0.21	0.35	r(2)
$CH_3CH{=}CHCHO(g) + * \leftrightarrow CH_3CH{=}CHCHO*$	−1.96	NaN	NaN	r(3)
$CH_3CH{=}CHCHO* + H* \leftrightarrow CH_3CH{=}CHCHOH* + *$	0.40	0.50	0.09	r(4)
$CH_3CH{=}CHCHOH* + H* \leftrightarrow CH_3CH{=}CHCH_2OH* + *$	−0.50	0.05	0.55	r(5)
$CH_3CH{=}CHCHOH* \leftrightarrow CH_3CH{=}CHCH_2OH(g) + *$	−1.38	NaN	NaN	r(6)
$CH_3CH{=}CHCH_2OH* + H* \leftrightarrow CH_3CH{-}CH_2CH_2OH* + *$	−0.44	0.50	0.94	r(7)
$CH_3CH{-}CH_2CH_2OH* + H* \leftrightarrow CH_3CH_2CH_2CH_2OH* + *$	−0.66	0.84	1.51	r(8)
$CH_3CH{=}CHCHO* + H* \leftrightarrow CH_3CH{-}CH_2CHO* + *$	0.32	0.75	0.43	r(9)
$CH_3CH{-}CH_2CHO* + H* \leftrightarrow CH_3CH_2{-}CH_2CHO* + *$	−1.50	0.32	1.82	r(10)
$CH_3CH_2{-}CH_2CHO* \leftrightarrow CH_3CH_2{-}CH_2CHO(g) + *$	−1.95	NaN	NaN	r(11)
$CH_3CH_2{-}CH_2CHO* + H* \leftrightarrow CH_3CH_2{-}CH_2CHOH* + *$	0.65	1.06	0.41	r(12)
$CH_3CH{-}CH_2CHOH* + H* \leftrightarrow CH_3CH_2{-}CH_2CH_2OH* + *$	−0.47	1.08	1.55	r(13)
$CH_3CH_2CH_2CH_2OH* \leftrightarrow CH_3CH_2CH_2CH_2OH(g) + *$	−1.20	NaN	NaN	r(14)

Microkinetic Simulations. Based on the aforementioned results, microkinetic simulations were further conducted to gain insights into the activity and selectivity trends of $Ti_1Au(320)$ and $Ti_1Au(111)$ surfaces in the selective hydrogenation of CRAL. A comprehensive microkinetic

modeling approach with a total of 14 elementary reaction steps associated with the two reaction pathways (as listed in table 1) were conducted. The coverage of each surface intermediate was calculated by solving the corresponding differential equations using the mkmcxx 2.15.3 software, enabling a detailed analysis of the reaction kinetics and intermediate species during the catalytic process.[46,47] As shown in Figure 6c, the production rate of CROL significantly surpasses that of BUAL and BUOL right from the start and the CROL maintains its dominance until equilibrium is reached after a period of 4 $\times 10^{-6}$s. In other words, the production rate of CROL greatly outpaces that of BUAL and BUOL, indicating an exceptionally high selectivity towards CROL. Figure 6d depicts the formation rates of the products (CROL, BUAL, and BUOL) as a function of temperature. Within the temperature range of 273 to 553 K, the production rates of both BUAL and BUOL show a gradual increase. However, the production rate of CROL greatly outpaces those of BUAL and BUOL at all temperatures by a significant margin. As a result, the selectivity analysis demonstrates a high selectivity towards CROL (Figure 6e). Moreover, the results observed on the (111) surface (Figures S55–S57) are consistent with those on the (320) surface. We conducted a comparison between the microkinetic simulation results of Ti_1Au SAA catalysts and the catalytic performance of Pd-Ag SAA reported in previous experimental studies.[25] The experimental data indicated that the reaction rate on Pd-Ag SAA is approximately 1×10^{-5} mol·s^{-1} at 5 atm pressure and 473 K, while our simulation results reveal that the reaction rate on $Ti_1Au(111)$ surface is approximately 2.35×10^{-5} mol·s^{-1} even at 2 atm pressure and 473 K. A noteworthy observation is that the selectivity to CROL on the Pd-Ag SAA catalyst is merely 31%, whereas our simulation results demonstrate that the selectivity to CROL on the $Ti_1Au(111)$ surface is close to 100%, further supporting the potential of Ti_1Au catalysts as high-performance candidate for the selective hydrogenation of CRAL.

■ CONCLUSION

DFT calculations and ML techniques are employed to systematically investigate the adsorption preference of crotonaldehyde on diverse SAA surfaces. By conducting three iterative rounds of ML using the Gaussian process regression (GPR) algorithm, 528 adsorption energies were accurately predicted with low errors of about 0.10 eV. The ML results revealed that the binding energy for the π_{CC} and π_{CO} adsorption modes is significantly influenced by the activation energy (*E*_s) and coordination number (CN), respectively. Notably, the Ti_1Au SAA, distinguished by the substantial variance in adsorption energy between the two modes, emerges as a most promising catalyst for CRAL reduction. Furthermore, DFT calculations confirmed the low hydrogenation energy barriers for C=O bonds (below 0.60 eV) on the Ti_1Au (320) and Ti_1Au (111) surfaces, underscoring their exceptional catalytic activity. Microkinetic simulations further validated the remarkable selectivity of crotyl alcohol (CROL), nearing 100%, on these surfaces within the temperature range of 373 to 553 K. These findings highlight the promising application potential of Ti_1Au SAA in the selective hydrogenation of unsaturated aldehyde. The present study, which integrates theoretical calculations and data-driven approach, paves the way for efficient and targeted exploration in catalyst design.

■ ASSOCIATED CONTENT

Supporting Information

The Supporting Information is available free of charge at http://pubs.acs.org.

Figure of Initial feature Pearson correlation coefficient matrix heat maps, comparison of four algorithms, three rounds of machine learning prediction results, the data distribution, charge density difference plot, PDOS, *d*-band center and COHP plot, comparison of DFT-calculated Gibbs free energy change values, intermediates and transition states structures, microkinetic simulations results on $Ti_1Au(111)$ surface, and tables of structural parameters, atomic parameters as inputs in the ML model, Gibbs

free adsorption energy of crotonaldehyde on SAA surfaces obtained by DFT calculation, and detailed parameters of four ML models.

■ AUTHOR INFORMATION

Corresponding Authors:

Jing Yang - *Institute of High Performance Computing (IHPC), Agency for Science, Technology and Research (A*STAR), 1 Fusionopolis Way, #16-16 Connexis, Singapore 138632, Republic of Singapore.* E-mail: Yang_Jing@ihpc.a-star.edu.sg

Xin Zhang - *State Key Laboratory of Chemical Resource Engineering, Beijing Advanced Innovation Center for Soft Matter Science and Engineering, Beijing University of Chemical Technology, Beijing 100029, P. R. China*; orcid.org/0000-0003-3559-2096; E-mail: zhangxin@mail.buct.edu.cn

Yong-Wei Zhang - *Institute of High Performance Computing (IHPC), Agency for Science, Technology and Research (A*STAR), 1 Fusionopolis Way, #16-16 Connexis, Singapore 138632, Republic of Singapore.* E-mail: zhangyw@ihpc.a-star.edu.sg

Authors

Haisong Feng - *State Key Laboratory of Chemical Resource Engineering, Beijing Advanced Innovation Center for Soft Matter Science and Engineering, Beijing University of Chemical Technology, Beijing 100029, P. R. China; Institute of High Performance Computing (IHPC), Agency for Science, Technology and Research (A*STAR), 1 Fusionopolis Way, Singapore 138632, Republic of Singapore*

Meng Zhang - *State Key Laboratory of Chemical Resource Engineering, Beijing Advanced Innovation Center for Soft Matter Science and Engineering, Beijing University of Chemical Technology, Beijing 100029, P. R. China*

Zhen Ge - *State Key Laboratory of Chemical Resource Engineering, Beijing Advanced Innovation Center for Soft Matter Science and Engineering, Beijing University of Chemical Technology, Beijing 100029, P. R. China*

Yuan Deng - *State Key Laboratory of Chemical Resource Engineering, Beijing Advanced Innovation Center for Soft Matter Science and Engineering, Beijing University of Chemical Technology, Beijing 100029, P. R. China*

Pengxin Pu - *State Key Laboratory of Chemical Resource Engineering, Beijing Advanced Innovation Center for Soft Matter Science and Engineering, Beijing University of Chemical Technology, Beijing 100029, P. R. China*

Wenyu Zhou - *School of Chemistry and Chemical Engineering, Chongqing Key Laboratory of Theoretical and Computational Chemistry, Chongqing University, Chongqing 401331, P. R. China; Institute of High Performance Computing (IHPC), Agency for Science, Technology and Research (A*STAR), 1 Fusionopolis Way, Singapore 138632, Republic of Singapore*

Hao Yuan - *Institute of High Performance Computing (IHPC), Agency for Science, Technology and Research (A*STAR), 1 Fusionopolis Way, #16-16 Connexis, Singapore 138632, Republic of Singapore.*

Feng Li - *State Key Laboratory of Chemical Resource Engineering, Beijing Advanced Innovation Center for Soft Matter Science and Engineering, Beijing University of Chemical Technology, Beijing 100029, P. R. China*

Notes

The authors declare no competing financial interest.

■ ACKNOWLEDGMENTS

This work was supported by the National Natural Science Foundation of China (22173003), the China Scholarship Council (No. 202206880016), the Italy-Singapore Science and Technology Cooperation (Grant No. R23101R040), and Singapore A*STAR SERC CRF Award. The use of computing resources at the A*STAR Computational Resource Centre and National Supercomputer Centre, Singapore is gratefully acknowledged.

■ REFERENCES

1. Vogt, C.; Weckhuysen, B. M. The Concept of Active Site In Heterogeneous Catalysis. *Nat. Rev. Chem.* **2022**, *6*, 89–111.

2. He, X.; He, Q.; Deng, Y.; Peng, M.; Chen, H.; Zhang, Y.; Yao, S.; Zhang, M.; Xiao, D.; Ma, D.; Ge, B.; Ji, H. A Versatile Route to Fabricate Single Atom Catalysts with High Chemoselectivity and Regioselectivity in Hydrogenation. *Nat. Commun.* **2019**, *10*, 3663.

3. Guan, Q.; Zhu, C.; Yu, H.; Zhang, X.; Liu, X.; Zhang, M.; Li, W.; Lu, J.; Lin, Y.; Cao, L.; Wang, H.; Vovk, E. I.; Zhou, X.; Yang, Y.; Wei, S. Bimetallic Monolayer Catalyst Breaks the Activity–Selectivity Trade-Off on Metal Particle Size for Efficient Chemoselective Hydrogenations. *Nat. Catal.* **2021**, *4*, 840–849.

4. Bunting, R. J.; Wodaczek, F.; Torabi, T.; Cheng, B. Reactivity of Single-Atom Alloy Nanoparticles: Modeling the Dehydrogenation of Propane. *J. Am. Chem. Soc.* **2023**, *145*, 14894−14902.

5. Feng, Q.; Zhao, S.; Wang, Y.; Dong, J.; Chen, W.; He, D.; Wang, D.; Yang, J.; Zhu, Y.; Zhu, H.; Gu, L.; Li, Z.; Liu, Y.; Yu, R.; Li, J. Li, Y. Isolated Single-Atom Pd Sites in Intermetallic Nanostructures: High Catalytic Selectivity for Semihydrogenation of Alkynes. *J. Am. Chem. Soc.* **2017**, *139*, 7294–7301.

6. Chen, X.; Shi, C.; Liang, C. Highly Selective Catalysts for the Hydrogenation of Alkynols: A Review. *Chinese J. Catal.* **2021**, *42*, 2105–2121.

7. Gu, Y.; Norton, J. R.; Salahi, F.; Lisnyak, V. G.; Zhou, Z.; Snyder, S. A. Highly Selective Hydrogenation of C═C Bonds Catalyzed by A Rhodium Hydride. *J. Am. Chem. Soc.* **2021**, *143*, 9657−9663.

8. Jiang, X.; Tang, L.; Dong, L.; Sheng, X.; Zhang, W.; Liu, Z.; Shen, J.; Jiang, H.; Li, C. Cu Single-Atom Catalysts for High-Selectivity Electrocatalytic Acetylene Semihydrogenation. *Angew. Chem. Int. Ed.* **2023**, e202307848.

9. Johar., P.; McElroy, C. R.; Rylott, E. L.; Matharu, A. S.; Clark, J. H. Biologically Bound Nickel as A Sustainable Catalyst for the Selective Hydrogenation of Cinnamaldehyde. *Appl. Catal. B-Environ.* **2022**, *306*, 121105.

10. Zhang, L.; Zhou, M.; Wang, A.; Zhang, T. Selective Hydrogenation over Supported Metal Catalysts: From Nanoparticles to Single Atoms. *Chem. Rev.* **2020**, *120*, 2, 683–733.

11. Luneau, M.; Lim, J.; Patel, D. A.; Sykes, E. C. H.; Friend, C. M.; Sautet, P. Guidelines to

Achieving High Selectivity for The Hydrogenation of α,β-Unsaturated Aldehydes with Bimetallic and Dilute Alloy Catalysts: A Review. *Chem. Rev.* **2020**, *120*, 12834−12872.

12. Yang, Y.; Rao, D.; Chen, Y.; Dong, S.; Wang, B.; Zhang, X.; Min, W. Selective Hydrogenation of Cinnamaldehyde over Co-based Intermetallic Compounds Derived from Layered Double Hydroxides. *ACS Catal.* **2018**, *8*, 11749−11760.

13. Yu, J.; Yang, Y.; Chen, L.; Li, Z.; Liu, W.; Xu. E.; Zhang, Y.; Hong, S.; Zhang, X. Min, W. NiBi Intermetallic Compounds Catalyst toward Selective Hydrogenation of Unsaturated Aldehydes. *Appl. Catal. B-Environ.* **2020**, *277*, 119273.

14. Zhang, Z.; Wang, Z.; Li, Z.; Zheng, W.; Fan, L.; Zhang, J.; Hu, Y.; Luo, M. F.; Wu, X. P.; Gong, X. Q.; Huang, W.; Lu, J. Q. Metal-Free Ceria Catalysis for Selective Hydrogenation of Crotonaldehyde. *ACS Catal.* **2020**, *10*, 14560–14566.

15. Wang, T.; Lan, X. Highly Selective Catalysts for The Hydrogenation of Unsaturated Aldehydes: A Review. *ACS Catal.* **2020**, *10*, 2764−2790.

16. Bai, S.; Bu, L.; Shao, Q.; Zhu, X.; Huang, X. Multicomponent Pt-based Zigzag Nanowires As Selectivity Controllers For Selective Hydrogenation Reactions. *J. Am. Chem. Soc.* **2018**, *140* 8384–8387.

17. Kahsar, K.R.; Schwartz, D.K.; Medlin, J.W. Control of Metal Catalyst Selectivity Through Specific Noncovalent Molecular Interactions. *J. Am. Chem. Soc.* **2014**, *136*, 520–526.

18. Guo, Z.; Xiao, C.; Maligal-Ganesh, R. V.; Zhou, L.; Goh, T. W.; Li, X.; Tesfagaber, D.; Thiel, A.; Huang, W. Pt Nanoclusters Confined within Metal−Organic Framework Cavities for Chemoselective Cinnamaldehyde Hydrogenation. *ACS Catal.* **2014**, *4*, 1340−1348.

19. Kahsar, K. R.; Schwartz, D. K.; Medlin, J. W. Control of Metal Catalyst Selectivity Through Specific Noncovalent Molecular Interactions. *J. Am. Chem. Soc.* **2014**, *136*, 520−526.

20. Wu, B.; Huang, H.; Yang, J.; Zheng, N.; Fu, G. Selective Hydrogenation of α,ß-Unsaturated Aldehydes Catalyzed by Amine-Capped Platinum-Cobalt Nanocrystals. *Angew. Chem., Int. Ed.* **2012**, *51*, 3440−3443.

21. Chiu, M. E.; Watson, D. J.; Kyriakou, G.; Tikhov, M. S.; Lambert, R. M. Tilt the Molecule and Change the Chemistry: Mechanism of S-Promoted Chemoselective Catalytic Hydrogenation of Crotonaldehyde on Cu(111). *Angew. Chem. Int. Ed.* **2006**, *45*, 7530−7534.

22. Jerdev, D. I.; Olivas, A.; Koel, B. E. Hydrogenation of Crotonaldehyde over Sn/Pt(111) Alloy Model Catalysts. *J. Catal.* **2002**, *205*, 278−288.

23. Koel, B. E. Structure, Characterization and Reactivity of Pt-Sn Surface Alloys. Model Systems in Catalysis: Single Crystals to Supported Enzyme Mimics. Springer: New York, 2010.

24. Cao, Y.; Chen, B.; Guerrero-Sanchez, J.; Lee, I.; Zhou, X.; Takeuchi, N.; Zaera, F. Controlling Selectivity in Unsaturated Aldehyde Hydrogenation Using Single-Site Alloy Catalysts. *ACS Catal.* **2019**, *9*, 9150−9157

25. Aich, P.; Wei, H.; Basan, B.; Kropf, A. J.; Schweitzer, N. M.; Marshall, C. L.; Miller, J. T.; Meyer, R. Single-Atom Alloy Pd−Ag Catalyst for Selective Hydrogenation of Acrolein. *J. Phys. Chem. C* **2015**, *119*, 18140−18148.

26. Loffreda, D. Theoretical Insight of Adsorption Thermodynamics of Multifunctional Molecules on Metal Surfaces. *Surf. Sci.* **2006**, *600*, 2103−2112.

27. Tuokko, S.; Pihko, P. M.; Honkala, K. First Principles Calculations for Hydrogenation of Acrolein on Pd and Pt: Chemo-selectivity Depends on Steric Effects on the Surface. *Angew. Chem., Int. Ed.* **2016**, *55*, 1670−1674.

28. Li, C.; Chen, Y.; Zhang, S.; Xu, S.; Zhou, J.; Wang, F.; Wei, M.; Evans, D. G.; Duan, X. Ni−In Intermetallic Nanocrystals as Efficient Catalysts toward Unsaturated Aldehydes Hydrogenation. *Chem. Mater.* **2013**, *25*, 3888−3896.

29. He, X.; Chen, Z. X.; Kang, G. J. Theoretical Study of the Role of Indium on the Selectivity of Acrolein Hydrogenation to Propenol on Gold Surfaces. *J. Phys. Chem. C* **2009**, *113*, 12325−12330.

30. Lucas, M.; Claus, P. Hydrogenations over Silver: A Highly Active and Chemoselective Ag-In/SiO2 Catalyst for the One-Step Synthesis of Allyl Alcohol from Acrolein. *Chem. Eng. Technol.* **2005**, *28*, 867−870.

31. Gutierrez, V.; Nador, F.; Radivoy, G.; Volpe, M. A. Highly Selective Copper Nanoparticles for the Hydrogenation of α,ß-Unsaturated Aldehydes in Liquid Phase. *Appl. Catal., A* **2013**, *464*, 109−115.

32. Muir, M.; Molina, D. L.; Islam, A.; Abdel-Rahman, M. K.; Trenary, M. Selective Hydrogenation of Acrolein on a Pd/Ag(111) Single-Atom Alloy Surface. *J. Phys. Chem. C* **2020**, *124*, 24271−24278.

33. Spivey, T. D.; Holewinski, A. Selective Interactions Between Free-Atom-Like *d*-States in Single-Atom Alloy Catalysts and Near-Frontier Molecular Orbitals. *J. Am. Chem. Soc.* **2021**, *143*,

11897−11902.

34. Tran, K.; Ulissi, Z. Active Learning Across Intermetallics to Guide Discovery of Electrocatalysts for CO_2 Reduction and H_2 Evolution. *Nat. Catal.* **2018**, *1*, 696–703.

35. Cao, L. Recent Advances in The Application of Machine-Learning Algorithms to Predict Adsorption Energies. *Trends Chem.* 2022, 4, 347–360.

36. Li, X.; Yang, Z.; Chen, Z.; Gao, W.; Jiang, Q. A Transferable Machine-Learning Scheme from Pure Metals to Alloys for Predicting Adsorption Energies. *J. Mater. Chem*. *A* **2022**, *10*, 872-880.

37. Kim, M.; Ha, M. Y.; Jung, W. B.; Yoon, J.; Shin, E.; Kim, Il.; Lee, W. B. Kim, Y.; Jung, H. Searching for an Optimal Multi-Metallic Alloy Catalyst by Active Learning Combined with Experiments. *Adv. Mater.* **2022**, *34*, 2108900.

38. Nugraha, A. S.; Lambard, G.; Na, J.; Hossain, M. S. A.; Asahi, T.; Chaikittisilp, W.; Yamauchi, Y. Mesoporous Trimetallic Ptpdau Alloy Films toward Enhanced Electrocatalytic Activity in Methanol Oxidation: Unexpected Chemical Compositions Discovered by Bayesian Optimization. *J. Mater. Chem. A* **2020**, *8*, 13532–13540.

39. Kim, M.; Kim, Y. Ha, M. Y.; Shin, E.; Kwak, S. J.; Park, M.; Kim, Il.; Jung, W. B.; Lee, W. B.; Kim, Y.; Jung, H. T. Exploring Optimal Water Splitting Bifunctional Alloy Catalyst by Pareto Active Learning. *Adv. Mater.* **2023**, *35*, 2211497.

40. Zhong, M.; Tran, K.; Min, Y.; Wang, C.; Wang, Z.; Dinh, C. T.; Luna, P. D.; Yu, Z.; Rasouli, A. S.; Brodersen, P.; Sun, S.; Voznyy, O.; Tan, C. S.; Askerka, M.; Che, F.; Liu, M.; Seifitokaldani, A.; Pang, Y.; Lo, S. C.; Ip, A.; Ulissi, Z.; Sargent, E. H. Accelerated Discovery of CO_2 Electrocatalysts Using Active Machine Learning. *Nature*, **2020**, *581*, 178–183.

41. Perdew, J. P.; Burke, K.; Ernzerhof, M. Generalized Gradient Approximation Made Simple. *Phys. Rev. Lett.* **1997**, *77*, 3865.

42. Kresse, G.; Furthmüller, J. Efficiency of Ab-Initio Total Energy Calculations for Metals and Semiconductors Using A Plane-Wave Basis Set. *Comput. Mater. Sci.* **1996**, *6*, 15−50.

43. Kresse, G.; Furthmüller, J. Efficient Iterative Schemes for Ab-Initio Total-Energy Calculations Using A Plane-Wave Basis Set. *Phys. Rev. B: Condens. Matter* **1996**, *54*, 11169−11186.

44. Grimme, S.; Antony, J.; Ehrlich, S.; Krieg, H. A Consistent and Accurate Ab Initio Parametrization of Density Functional Dispersion Correction (DFT-D) for the 94 Elements H-Pu. *J.*

Chem. Phys. **2010**, *132*, 154104.

45. Blöchl, P. Projector Augmented-Wave Method. *Phys. Rev. B: Condens. Matter* **1994**, *50*, 17953−17979.

46. Kresse, G.; Joubert, D. From Ultrasoft Pseudopotentials to the Projector Augmented-Wave Method. *Phys. Rev. B: Condens. Matter* **1999**, *59*, 1758−1775.

47. Henkelman, G.; Jónsson, H. A Dimer Method for Finding Saddle Points on High Dimensional Potential Surfaces Using Only First Derivatives. *J. Chem. Phys.* **1999**, *111*, 7010–7022.

48. Henkelman, G.; Uberuaga, B.; Jónsson, H. A Climbing Image Nudged Elastic Band Method for Finding Saddle Points And Minimum Energy Paths. *J. Chem. Phys.* **2000**, *113*, 9901−9904.

49. Michaelides, A.; Hu, P. Catalytic Water Formation on Platinum: A First-Principles Study. *J. Am. Chem. Soc.* **2001**, *123*, 4235−4242.

50. Cao, Y.; Guerrero-Sańchez, J.; Lee, I.; Zhou, X.; Takeuchi, N.; Zaera, F. Kinetic Study of the Hydrogenation of Unsaturated Aldehydes Promoted by Cuptx/SBA-15 Single-Atom Alloy (SAA) Catalysts. *ACS Catal.* **2020**, *10*, 3431−3443.

51. Pedregosa, F.; Varoquaux, G.; Gramfort, A.; Michel, V.; Thirion, B. Scikit-Learn: Machine Learning in Python. *J. Mach. Learn Res.* **2011**, *12*, 2825−2830.

52. Feng, H.; Ding, H.; Wang, S.; Deng, Y.; Yang, Y.; Wei, M.; Zhang, X. Machine-Learning-Assisted Catalytic Performance Predictions of Single-Atom Alloys for Acetylene Semihydrogenation. *ACS Appl. Mater. Interfaces* **2022**, *14*, 25288−25296.

53 Filot, I. A. W.; Broos, R. J. P.; van Rijn, J. P. M.; van Heugten, G. J. H.; van Santen, R. A.; Hensen, E. J. M. First-Principles-Based Microkinetics Simulations of Synthesis Gas Conversion on A Stepped Rhodium Surface. *ACS Catal.* **2015**, *5*, 5453−5467.

54. Filot, I. A. W.; van Santen, R. A.; Hensen, E. J. M. The Optimally Performing Fischer–Tropsch Catalyst. *Angew. Chem.* **2014**, *126*, 12960 –12964.

55. Hou, F.; Zhao, H.; Song, H.; Chou, L.; Zhao, J.; Yang, J.; Yan, L. Effect of Impregnation Strategy on Catalytic Hydrogenation Behavior of PtCo Catalysts Supported on $La_2O_2CO_3$ Nanorods. *J. Rare Earths* **2018**, *36*, 965−973.

56. Kliewer, C. J.; Bieri, M.; Somorjai, G. A. Hydrogenation of the α,ß-Unsaturated Aldehydes Acrolein, Crotonaldehyde, and Prenal over Pt Single Crystals: A Kinetic and Sum-Frequency

Generation Vibrational Spectroscopy Study. *J. Am. Chem. Soc.* **2009**, *131*, 9958−9966.

57. Chen, A.; Zhuang, X.; Chen, L.; Yao, S.; Zhou, Z. A Machine Learning Model on Simple Features for CO_2 Reduction Electrocatalysts. *J. Phys. Chem. C* **2020**, *124*, 22471−22478.

58. Lu, S.; Zhou, Q.; Ouyang, Y.; Guo, Y.; Li, Q.; Wang, J. Accelerated Discovery of Stable Lead-Free Hybrid Organic-Inorganic Perovskites Via Machine Learning. *Nat. Commun.* **2018**, *9*, 3405.

■ Table of Contents (TOC)